

Interaction between eddies and mean flow in Jupiter's atmosphere: Analysis of Cassini imaging data

Colette Salyk^{a,*}, Andrew P. Ingersoll^a, Jean Lorre^{b,✱}, Ashwin Vasavada^b, Anthony D. Del Genio^c

^a Division of Geological and Planetary Sciences, California Institute of Technology, MC 150-21, Pasadena, CA 91125, USA

^b Jet Propulsion Laboratory, California Institute of Technology, 4800 Oak Grove Drive, Pasadena, CA 91109, USA

^c NASA Goddard Institute for Space Studies, 2880 Broadway, New York, NY 10025, USA

Received 11 August 2005; revised 21 July 2006

Available online 23 October 2006

Abstract

Beebe et al. [Beebe, R.F., et al., 1980. *Geophys. Res. Lett.* 17, 1–4] and Ingersoll et al. [Ingersoll, A.P., et al., 1981. *J. Geophys. Res.* 86, 8733–8743] used images from Voyagers 1 and 2 to analyze the interaction between zonal winds and eddies in Jupiter's atmosphere. They reported a high positive correlation between Jupiter's eddy momentum flux, $\rho \overline{u'v'}$, and the variation of zonal velocity with latitude, $d\bar{u}/dy$. This correlation implied a surprisingly high rate of conversion of energy from eddies to zonal flow: $\sim 1.5\text{--}3.0 \text{ W m}^{-2}$, a value more than 10% of Jupiter's thermal flux emission. However, Sromovsky et al. [Sromovsky, L.A., et al., 1982. *J. Atmos. Sci.* 39, 1413–1432] argued that possible biases in the analysis could have caused an artificially high correlation. In addition, significant differences in the derived eddy flux between datasets put into question the robustness of any one result. We return to this long-standing puzzle using images of Jupiter from the Cassini flyby of December 2000. Our method is similar to previous analyses, but utilizes an automatic feature tracker instead of the human eye. The number of velocity vectors used in this analysis is over 200,000, compared to the 14,000 vectors used by Ingersoll et al. We also find a positive correlation between $\overline{u'v'}$ and $d\bar{u}/dy$ and derive a global average power per unit mass, $\overline{u'v'} d\bar{u}/dy$, ranging from $(7.1\text{--}12.3) \times 10^{-5} \text{ W kg}^{-1}$. Utilizing Ingersoll et al.'s estimate of the mass per unit area involved in the transport, this would imply a rate of energy conversion of $\sim 0.7\text{--}1.2 \text{ W m}^{-2}$. We discuss the implications of this result and employ several tests to demonstrate its robustness.

© 2006 Elsevier Inc. All rights reserved.

Keywords: Jupiter, atmosphere; Atmospheres, dynamics

1. Background

The eddy momentum flux (EMF) is an important element of atmospheric general circulations because it is involved in maintaining the mean zonal flow (e.g., Holton, 2004). The word “zonal” refers to longitude. A positive zonal velocity is a wind to the east. A zonal mean is an average with respect to longitude. An eddy is a departure from the zonal mean—a residual after the zonal mean has been subtracted off. Jupiter has at least seven eastward jets in each hemisphere. On Earth, one jet dominates each hemisphere. In this paper, the EMF refers to the northward transport of eastward momentum by the eddies—the

amount of eastward momentum transferred northward per unit area per unit time. The EMF is itself a zonal mean—an average with respect to longitude of all the individual fluxes around the latitude circle. The divergence of the EMF—its derivative with respect to the northward coordinate—is a force per unit volume that acts to decelerate the zonal wind at that latitude.

A negative divergence at the core of an eastward jet means that more momentum is entering the jet on its south side than is leaving the jet on its north side, so the jet is gaining eastward momentum. In this case, the jet is accelerated to the east. A positive divergence at the core of a westward jet means the jet is accelerated to the west. Equivalently, the eddies are transferring energy into eastward and westward jets when the EMF and the shear $d\bar{u}/dy$ have the same sign (Holton, 2004). Here \bar{u} is the mean zonal wind and y is the distance northward along a meridian. The EMF is $\rho \overline{u'v'}$, where u' and v' are the zonal

* Corresponding author.

E-mail address: csalyk@gps.caltech.edu (C. Salyk).

✱ Deceased.

(eastward) and meridional (northward) components of the eddy winds, respectively. Since $\rho v'$ is a northward eddy mass flux (mass per unit area per unit time), and u' is eastward eddy velocity (eastward momentum per unit mass), $\rho \overline{u'v'}$ is eastward momentum transported northward by the eddies per unit area per unit time.

In an observational study like ours, u' and v' are simply the departures from the zonal means \bar{u} and \bar{v} , respectively. However, these departures include both true eddy motions and measurement errors. (See Section 5.7 for a discussion of the effect of measurement errors on $\overline{u'v'}$.) The product $\overline{u'v'} d\bar{u}/dy P/g$ integrated over the surface area of the planet is the rate (power) at which energy is being transferred from eddies to the zonal jets. Here P/g is the mass per unit area of the layer in which this transfer is taking place, and $\overline{u'v'} d\bar{u}/dy$ is the power per unit mass of this transfer. The integrated product $\overline{u'v'} d\bar{u}/dy P/g$ could be positive or negative. In the latter case the eddies would be taking energy out of the jets. In the former case they would be putting it in.

By tracking cloud features in images of Jupiter from the Voyager missions, Beebe et al. (1980) and Ingersoll et al. (1981) found evidence that Jupiter's eddies were, indeed, supplying energy to the zonal wind flow. This was concluded after noting a positive correlation between the EMF and the variation of zonal velocity with latitude, $d\bar{u}/dy$. They calculated the power per unit area by considering a reference case—a layer with mass per unit area 10^4 kg m^{-2} , corresponding to a pressure difference of $\sim 2.5 \times 10^5 \text{ Pa}$. For this layer, they derived a power per unit area between 1.5 and 3 W m^{-2} . This implied that the rate of energy transfer from eddies to the zonal flow is more than 10% of Jupiter's emitted thermal radiation. On Earth, eddies are also observed to transfer energy into the zonal flow (e.g., DelSole, 2001; Holton, 2004), but at a rate that is only about 0.1% of Earth's emitted thermal radiation (Peixoto and Oort, 1992).

The analysis of Ingersoll et al. (1981), however, was quickly challenged by Sromovsky et al. (1982) who argued that sampling biases could skew the results of such a study. Among their concerns were the possibilities that a few, well-sampled areas of the planet were contributing disproportionately to the observed correlation, that the longitudinally averaged $\overline{u'v'}$ was strongly affected by values of $u'v'$ far from the median of the sample, and that the human eye, which was used for feature correlation, may have introduced unknown biases.

More than 20 yr later, Cassini provides an opportunity to revisit these issues. We report results of an analysis of EMF using images from the flyby of Jupiter in December 2000, analyzed with an automatic feature-tracker. The automatic tracker provides the advantages of more even planetary coverage, a greater number of tracked features, the absence of human bias, and greater flexibility for investigating the influence of sampling.

2. Observations and reduction

The dataset for this study consists of 38 1×2 North–South mosaics taken by the Cassini Imaging Science Subsystem Narrow Angle Camera during the spacecraft's flyby of Jupiter. The images were taken with the CB2 Filter, which is centered at

750 nm and has a full width of about 10 nm. This filter is a near infrared continuum band that sees through the methane and other gases to the tropospheric cloud features that were observed by Voyager at visible wavelengths. Unlike Saturn, where there is evidence that the altitude of the features used in cloud tracking has changed (Porco et al., 2005), Jupiter's features seem to stay at fairly constant altitude.

A mosaic was taken every 63 min, and the images span a $\sim 39 \text{ h}$ period from December 11–December 13, 2000, providing global coverage of nearly 4 rotations of the planet. During this time, the projected pixel size on the planet decreased from 122 to 114 km. The limb of Jupiter was fit to determine latitudes and longitudes to an accuracy of about a tenth of a pixel (see Section 5.7). Images were then flux-calibrated and photometrically corrected to account for sunlight differences across the planet. This was performed with a Minnaert correction with $k = 1$ for all images (Minnaert, 1941). The correction performed well except at regions far from the sub-solar or sub-spacecraft point; however, as discussed in later sections, these regions, corresponding to the edges of our images, were not included in our analysis. The photometric correction acts as a high-pass filter. Any residual large-scale brightness variations should not affect the identification of small-scale features. Based on measurement of flux variation in a featureless region of Jupiter's atmosphere, we estimate the flux noise to be less than 1% of the typical contrast seen between bright and dark regions of the atmosphere, so small-scale noise should not affect our analysis.

Finally, the images were cylindrically projected onto 1801×1801 pix arrays with a resolution of $0.1^\circ \text{ pix}^{-1}$, or $\sim 125 \text{ km pix}^{-1}$ at the equator. A sample raw image is plotted side-by-side with its calibrated, map-projected image, in Fig. 1. Note that the projected images are centered at 0° latitude even though each raw image covers only half of the planet's disk, such that approximately half of every map-projected image is empty. We do not show the empty, southern part of the projected image in Fig. 1.

The raw data, calibration software and map projection software used in this analysis are the same as that used by Porco et al. (2003) to determine Jupiter's zonal velocity profile.

3. Determination of wind flow

3.1. Feature tracking

The north and south components of the mosaics were analyzed separately. For each planetary rotation, each component produced a pair of images separated in time by approximately one planetary rotation period ($\sim 9.5 \text{ h}$), with centers offset by about 17° of longitude. The resulting 57 pairs of cylindrically-projected images were analyzed with an automatic feature-tracker developed by one of us (Lorre). The feature-tracker takes equally spaced boxes located at the vertices of a grid on one image and searches for a matching box on the second image. The tracking program's initial guess for the box's location on the second image was based on Jupiter's mean zonal velocity profile determined from Voyager images (Limaye, 1986).

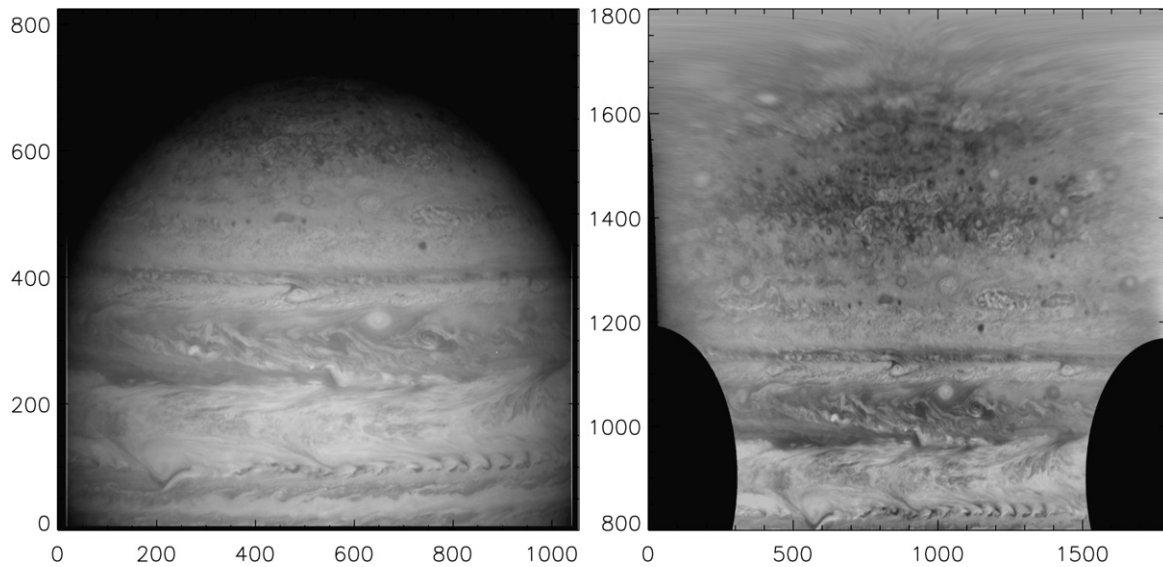


Fig. 1. A raw image on the left and a calibrated, projected image on the right.

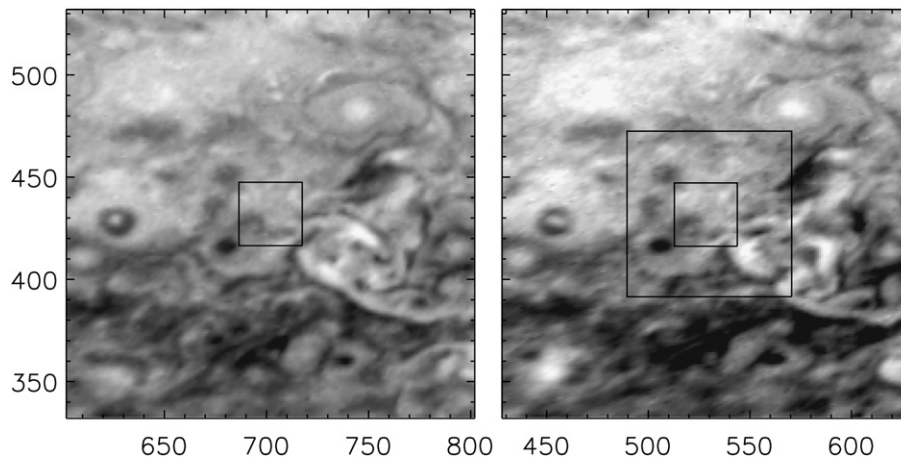


Fig. 2. One matched pair found by the feature tracker. The smaller of the two black boxes is the 31×31 pix correlation box, used by the feature tracker to calculate the correlation and determine the best match. The larger of the two black boxes is the total allowable search area: 81×81 pix. Extra image area is included for context, but was not used by the feature tracker.

The grid spacing, correlation box size, minimum level of acceptable correlation, and maximum search area can all be varied. The grid spacing was chosen to be small enough to resolve the main cloud features and jets, whose scales range from one to a few degrees. The correlation box size was chosen to be small enough to distinguish features while being large enough to keep noise and incorrect matches low. Ideally, the correlation box would be much smaller and the time interval would be much shorter than the size and variation timescale of the cloud features, but the data set does not allow this. We are therefore not resolving the small, rapidly-varying eddies. For the nominal case, the grid spacing was 10 pix, the correlation box was 31×31 pix, the total search area for each point was 81×81 pix and the minimum allowed correlation coefficient between the two boxes was 0.8. The feature tracker also has an option that allows one to start with the matched box on the second image and work backwards to find a box on the first. One can then specify by how much the starting point and backwards found box may differ to remain in the analysis.

This backwards search criterion allows the feature tracker to judge the quality of the match it has chosen in relation to other possible matches in the vicinity. If the feature tracker can find several nearly equal quality matches within the search region, it is more likely to choose different matches in the forwards and backwards direction. For our nominal analysis, a displacement of more than 2 pix between the starting search location and the location found by working backwards resulted in the exclusion of that match. About 26% of the matches were eliminated in this way.

Fig. 2 shows a match found by the feature tracker, demonstrating the size of the correlation box and the total search area. Variations in grid spacing and correlation box size cause only small changes in the analysis, so long as they remain within reasonable ranges as determined by the size of cloud features. Our methods and parameters are similar to those of Vasavada et al. (1998), who used an earlier version of the feature tracker to derive the flow fields around specific bands and major vortices as seen by Galileo. In Section 5, we discuss the effect of varying

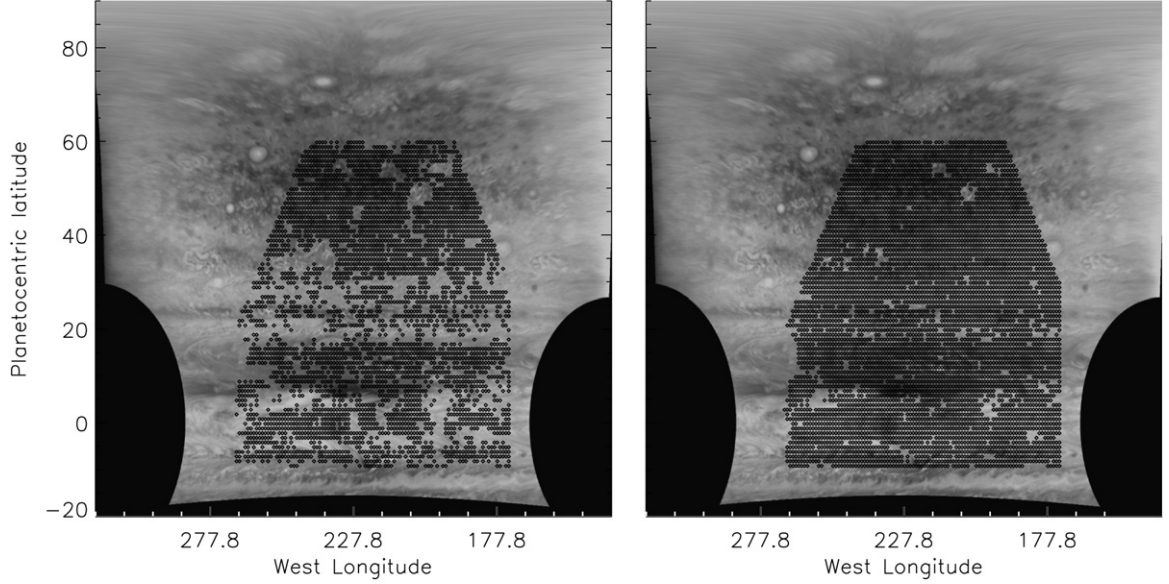


Fig. 3. Sample cylindrically-projected map from a single image with location of matched points plotted in black. On the left, points are from our nominal analysis, in which the feature tracker utilized stringent acceptance criteria; on the right, points are from our analysis with more complete coverage of the planet (see Section 5.2). The sharp edges of the distribution represent the limits we set to eliminate the low-resolution portions of the maps. Gaps tend to correspond to busy regions, in which features change significantly in the time between images of a pair.

the minimum level of acceptable correlation and of not using the backwards elimination feature.

The feature tracker typically yielded several thousand pairs of points representing the positions of the correlated boxes on the two images separated in time. We empirically determined that the wind vectors on the edges of the images were unreliable due to a loss of resolution. We eliminated all vectors beyond $\pm 60^\circ$ latitude, as well as those more than 55° away from the meridian at the equator, up to as little as 34° away from the meridian at the poles. A sample image overlaid with the locations of points used in our nominal analysis is shown on the left-hand side of Fig. 3. The pairs remaining after the removal of the image edges were then screened by a simple program designed to remove spurious matches. Spurious matches were generally the result of the feature tracker jumping from one feature to a similar feature nearby, and were easy to identify by eye. We designed our screening process to eliminate such jumps, and therefore chose lenient elimination criteria, so as to limit the exclusion of real data. Each $(\Delta x, \Delta y)$ (where Δ refers to the distance, in pixels, between the two image pairs in the x and y directions and x includes a component due to longitude offset) was compared with up to eight of its neighbors in the longitudinal direction. It was removed from the analysis if its Δx differed from the mean of its neighbors by more than 25% or if its Δy was greater than 4 pix. 4 pix in the y direction corresponds to velocities of about 15 m s^{-1} , while eddy velocities in the y -direction tend to be in the range of $2\text{--}4 \text{ m s}^{-1}$. The x -direction elimination criterion implies more than 100 m s^{-1} difference in velocity between one point and its neighbors. A small number, about 1%, of matches were eliminated by this screening process. For the dataset presented here, the total number of pairs remaining after this step was 201,134.

Position and time information were used to convert these pairs to wind vectors of the form $\mathbf{u}_i = u_i \hat{\mathbf{x}} + v_i \hat{\mathbf{y}}$, where x and y are eastward and northward coordinates, respectively, and i is the index of a single measurement. The vectors were then used to determine zonal mean velocities in 1° latitude bins. Since our correlation box is 3° on a side, we are over-sampling in both latitude and longitude by a factor of 3.

3.2. Notation

Following Ingersoll et al. (1981), we define the zonally-averaged winds for a 1° latitude bin as

$$\bar{u}_n = \frac{1}{I} \sum_{i=1}^I u_i \quad \text{and} \quad \bar{v}_n = \frac{1}{I} \sum_{i=1}^I v_i, \quad (1)$$

where n is the index of a given latitude bin and I is the total number of wind vectors in that bin. For our nominal analysis, u_i and v_i are individual vectors which may come from any longitude. Thus, this mean is potentially biased if features are easier to identify and track at some longitudes than at others. We discuss this issue further in Section 5.2.

We then define the eddy (non-zonal) components of the winds as

$$u'_i = u_i - \bar{u}_n \quad \text{and} \quad v'_i = v_i - \bar{v}_n. \quad (2)$$

Note that u'_i and v'_i represent all deviations from mean measured motions and therefore will include random and systematic errors along with true eddy motion.

Finally, we define the longitudinally averaged eddy momentum flux for a given latitude bin:

$$\overline{u'v'}_n = \frac{1}{I} \sum_{i=1}^I u'_i v'_i \quad (3)$$

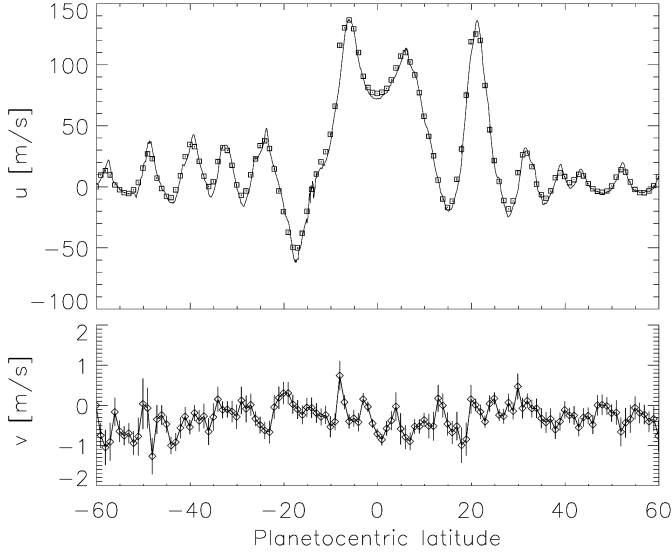


Fig. 4. \bar{u} and \bar{v} are plotted as a function of latitude for our nominal analysis. Error bars are 2 standard deviations from the mean. For the \bar{u} plot, the error bars are smaller than the box symbols, though actual errors may be larger due to systematics. \bar{u} is also compared with the zonal velocity profile of Porco et al. (2003). There is good agreement between the two curves, except for discrepancies at the sharpest peaks, due to our relatively larger grid spacing.

as well as the variation of zonal velocity with latitude:

$$\left(\frac{d\bar{u}}{dy}\right)_n = \frac{\bar{u}_{n+1} - \bar{u}_{n-1}}{y_{n+1} - y_{n-1}}. \quad (4)$$

4. Results

4.1. Rate of energy conversion

Fig. 4 shows \bar{u} and \bar{v} as a function of latitude for our nominal analysis, with \bar{u} overplotted on the zonal velocity profile of Porco et al. (2003). There is fairly good agreement between these two curves, despite the fact that Porco et al. used a line-by-line correlation method, rather than a feature tracker, to determine \bar{u} . The largest differences between the two curves exist at the most extreme \bar{u} values where our wind profile is smoothed slightly due to our coarser grid resolution. \bar{v} is slightly offset from zero, with a mean value of -0.2 m s^{-1} . Although this may be a real effect, a non-zero \bar{v} has not been noted by previous researchers and could be induced by a small navigation error, which we discuss further in Section 5.7.

Fig. 5 shows $d\bar{u}/dy$, $\overline{u'v'}$, and their product as a function of latitude. We note a positive correlation between the signs of these two parameters, implying a flow of energy from eddies to zonal flow. The correlation coefficient of the bottom curves is ~ 0.86 .

Following the convention of Holton (2004), the rate of transfer of eddy kinetic energy (K') to zonal mean kinetic energy (\bar{K}) is defined as

$$[K' \bullet \bar{K}] \equiv \left\langle \rho \overline{u'v'} \frac{d\bar{u}}{dy} \right\rangle, \quad (5)$$

where $\langle \rangle$ represents a global average. Our measurements allow us to estimate the product $\overline{u'v'} d\bar{u}/dy$, which, when averaged

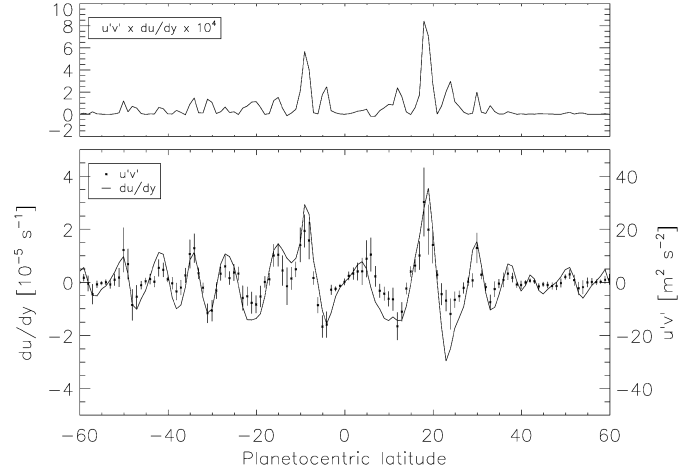


Fig. 5. On the bottom plot, $\overline{u'v'}$ and $d\bar{u}/dy$ are plotted together as a function of latitude. $\overline{u'v'}$, corresponding to the right of the two axes, is plotted as dots with error bars corresponding to 2 standard deviations from the mean. $d\bar{u}/dy$ is shown as a solid line and corresponds to the left of the two axes. There is a distinct positive correlation between the two curves, and their correlation coefficient is 0.86. The top plot shows the product $\overline{u'v'} \times d\bar{u}/dy$.

Table 1

Type of analysis	Correlation between $d\bar{u}/dy$ and $\overline{u'v'}$	Power/mass ($10^{-5} \text{ W kg}^{-1}$)	2σ error
Conservative	0.86	7.1	0.66
Conservative, no ovals	0.87	7.1	0.76
Conservative, binned	0.87	7.3	0.59
More complete	0.88	12.3	0.59
More complete, no ovals	0.87	12.3	0.80
More complete, binned	0.87	12.4	0.70
Two rotations, cons.	0.74	6.0	1.4
Artificial shear	0.56	0.33	0.37
Ingersoll et al. (1981)	0.4–0.5	15–30	

over the surface yields the power per unit mass transferred from eddies to zonal mean flow. Letting n refer to a given latitude bin and N be the total number of bins, this power per unit mass is given by

$$\text{power/mass} \approx \frac{1}{\sum_{n=1}^N \cos \phi_n} \sum_{n=1}^N \left(\frac{d\bar{u}}{dy} \right)_n (\overline{u'v'})_n \cos \phi_n. \quad (6)$$

For our nominal analysis, this quantity is equal to $7.1 \times 10^{-5} \text{ W kg}^{-1}$, compared to a value of $15\text{--}30 \times 10^{-5} \text{ W kg}^{-1}$ found by Ingersoll et al. (1981). We performed several, slightly different analyses, which will be discussed in Section 5, and the power per unit mass derived from all analyses can be viewed in Table 1.

In order to estimate the total power transfer from eddies to zonal flow, it is necessary to know the amount of mass involved in the transfer. Multiplying power per unit mass by the mass per unit area dP/g , one can obtain the total power per unit area transferred—a number that can be compared to the total power per unit area emitted by the planet. Unfortunately, the mass involved in the transfer is not well constrained; dP is uncertain to perhaps an order of magnitude. At a minimum, the transfer includes the main visible cloud deck, which has been estimated to depths just short of 1 bar (Atreya and Donahue, 1979; Kunde et al., 1982; Banfield et al., 1998) or to between 1 and

2 bar (e.g., Irwin et al., 2001). However, the transfer likely extends much deeper. Ingersoll et al. (1981) utilized a value for dP/g of 10^4 kg m^{-2} (the mass per unit area in a layer 2.5 bar thick) as a convenient reference number. If we use this value for the mass per unit area, the product of dP/g times the power per unit mass is thus 0.71 W m^{-2} , or about 2–4 times less than that found by Ingersoll et al. This is about 5% of Jupiter's thermal energy release.

4.2. Estimates of error

The error bars shown in Fig. 5 are two-sigma estimates of the error of the mean, and are given by $2\sigma(u'v')\sqrt{3/I}$. Here $\sigma(u'v')$ is the standard deviation of the individual measured $u'v'$ values and $I/3$ is the number of degrees of freedom (the factor of 3 arises because the measurements overlap by a factor of 3 in longitude). Equation (7) of Ingersoll et al. (1981) gives the contribution of measurement errors to the variance of $u'v'$; the expression goes to zero when the measurement error goes to zero. To get the full variance, one must add the contribution of the true wind variations—the variance of the true $u'v'$ values from their mean divided by the number of degrees of freedom. This variance could be quite large, since the flow is chaotic and the wind vectors go in all directions. Limaye et al. (1982) estimate that true wind variations make the largest contribution to the variance of $u'v'$, followed by feature tracking errors, and then by errors of navigation. The error bars in Fig. 5 reflect all three sources of uncertainty. $\sigma(u'v')$ is typically around $20\text{--}30 \text{ m}^2 \text{ s}^{-2}$, though it approaches $\sim 100 \text{ m}^2 \text{ s}^{-2}$ at some latitudes. The number of measurements, I , in a given 1° latitude bin is typically 1600. This means that $\sigma_{uv} \lesssim 4 \text{ m}^2 \text{ s}^{-2}$, which is less than the signal plotted in Fig. 5 by an order of magnitude. In all figures showing $\overline{u'v'}$, we use this error estimate to plot a 2σ error bar. Errors in $d\overline{u}/dy$ are a couple of orders of magnitude smaller than errors in $\overline{u'v'}$ because errors in \overline{u} are small (of order $\sim \text{few} \times 0.1 \text{ m s}^{-1}$) and get divided by a large dy , so the major contributor to the error in power/mass is σ_{uv} . We propagate this error through Eq. (6); errors appear in the last column of Table 1. Note that these statistical errors are much smaller than the variation in power/mass between analyses, which suggests the importance of systematic errors and different standards for accepting or rejecting data. Systematic effects are discussed in detail in Section 5.

4.3. Comparison with other studies

The three other studies of the EMF in Jupiter's atmosphere are Beebe et al. (1980), Ingersoll et al. (1981), and Sromovsky et al. (1982). A companion paper by Limaye et al. (1982) describes the data and methods used by Sromovsky et al. (1982). All used Voyager data, and all used manual feature tracking to measure winds. Beebe et al. (1980) used Voyager 1 orange-filter images at 80 km pix^{-1} resolution. Ingersoll et al. (1981) added Voyager 2 violet-filter images at 65 km pix^{-1} resolution. The resolution of the images used by Limaye et al. (1982) and Sromovsky et al. (1982) was 280 km pix^{-1} . Beebe et al. (1980) and Ingersoll et al. (1981) tracked clouds in pairs of raw (not

map projected) images separated by one planetary rotation using the AMOS system at the Jet Propulsion Laboratory. Limaye et al. (1982) and Sromovsky et al. (1982) tracked clouds in triplets of images spanning two planetary rotations using the McIDAS system at the University of Wisconsin. Their data were a set of cylindrical projection mosaics generated at the Jet Propulsion Laboratory from Voyager 2 violet-filter images.

For manual tracking with image pairs, Ingersoll et al. (1981) estimate the uncertainty of feature identification as 2 pix, or 130 km, in their study. For manual tracking with image triplets, Limaye et al. (1982) estimate the uncertainty as ~ 1 pix or 280 km in their study. In the present study, we tracked features forward and backward in time and eliminated those whose positions differed by more than 2 pix (260 km), so the uncertainty is less than this number.

Resolution, which is different from uncertainty, is difficult to compare. With manual feature tracking, one can identify features as small as one or two pixels, but the features may be 10–40 pix apart and irregularly spaced. With automatic feature tracking, we identify features by the correlation box, which is 3° on a side, or 3740 km at the equator, but we record velocities on a $1^\circ \times 1^\circ$ grid. Thus manual feature tracking can detect relatively small-scale features and measure their speed, but the spatial sampling is irregular and can be quite sparse. Automatic feature tracking can detect features larger than the correlation box and measure their speed, and the spatial sampling is regular. Since we oversample in space, our 201,134 velocity vectors are equivalent to $201,134/9 = 22,348$ independent velocity vectors between $\pm 60^\circ$ latitude. The vectors are spread out over ~ 4 rotations of the planet. Sromovsky et al. (1982) had 8190 vectors, and Ingersoll et al. (1981) had 6933 and 7177 vectors for Voyagers 1 and 2, respectively, and they are spread out over space and time intervals comparable to those in the present study.

In their initial estimate of $\overline{u'v'}/d\overline{u}/dy$, Limaye et al. (1982) and Sromovsky et al. (1982) appear to confirm the finding of large eddy-to-mean-flow conversion rates. Beebe et al. (1980) and Ingersoll et al. (1981) assume that a layer 2.5 bar thick, or 10^4 kg m^{-2} in mass, is involved in the transfer. Their conversion rate is 3.3 W m^{-2} , which is greater than the 2.9 W m^{-2} for Voyager 1 (Beebe et al., 1980) and 1.1 W m^{-2} for Voyager 2 (Ingersoll et al., 1981). Sromovsky et al. point out that the differences between these numbers are not likely to be real, and are probably due to the different sampling strategies of the individuals making the measurements. In our Cassini study, we find a conversion rate in the range $0.7\text{--}1.2 \text{ W m}^{-2}$, depending on the criteria used for accepting or rejecting data.

In an analysis of their own data, Sromovsky et al. (1982) argue that the correlation of $\overline{u'v'}$ and $d\overline{u}/dy$ is probably caused by a biased sampling of prominent cloud features associated with circulating eddies. They did some intensive diagnostic measurements of selected areas, where they applied more nearly uniform spatial sampling, and found no significant correlation. They argue that the next step is to process the entire data set with uniform spatial density at high spatial resolution. With our automatic feature tracker, we can achieve the former but not the latter. Although the Voyager resolution is $\sim 65 \text{ km/pix}$ compared to $\sim 120 \text{ km/pix}$ for Cassini, the actual resolutions are

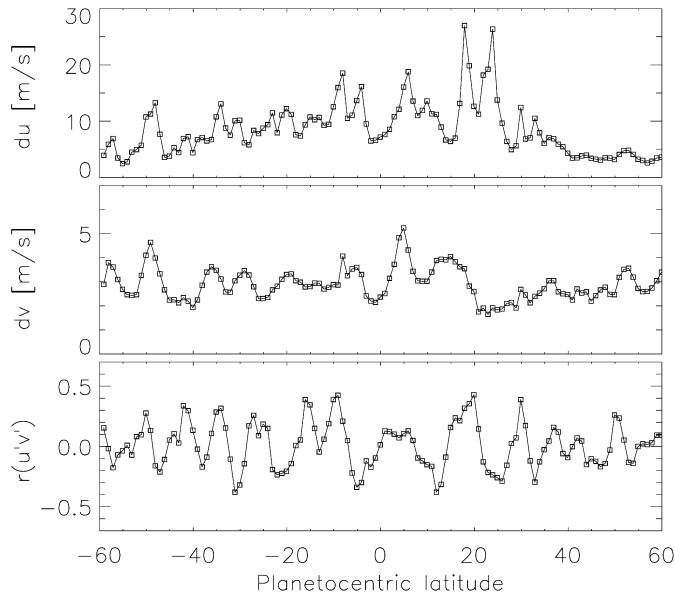


Fig. 6. δu , δv and $r(u'v')$ are plotted as a function of latitude. Note the different y-axis scales for δu and δv .

comparable, because Voyager's point spread function is wider than one pixel. We choose features based on their location relative to a latitude–longitude grid; we do not choose them for their individuality, so we need a large correlation box to define them uniquely. We achieve nearly uniform spatial sampling and, as shown below (Section 5.3), we can eliminate the large circulating eddies and get nearly the same results.

The large size of the correlation box in our study probably accounts for a significant difference between our results and those obtained by manual feature tracking: The root mean square eddy velocities δu and δv are of order 8 and 3 m s^{-1} , respectively, in our study. These are 1/3 to 2/3 the values reported in the earlier studies. Apparently much of the kinetic energy is at scales below the size of our correlation box. These motions get averaged out in our study, but they are sampled (irregularly) in the studies that use manual feature tracking.

The smallness of the eddy velocities δu and δv is consistent with the smallness of $\overline{u'v'}$ in our study. The correlation coefficient $r(u'v')$, defined as $\overline{u'v'}/(\delta u \delta v)$, is about the same as in Ingersoll et al. (1981). Fig. 6 shows this relationship. At most latitudes, $r(u'v')$ oscillates between ± 0.4 , which is the same as in Fig. 9 of Ingersoll et al. (1981). The difference is that δv and δu are smaller than the values plotted in Figs. 5 and 6 of Ingersoll et al. (1981). Interestingly, δv has the same tapered shape with a maximum at low latitudes, and δu has the same flat shape independent of latitude in both studies.

The values of $\overline{u'v'}$, δu , δv , $d\bar{u}/dy$, and $r(u'v')$ for Jupiter are not too different from (0.5 to 2.0 times) the values for Earth. On Earth the peak value of $\overline{u'v'}$ is $\sim 40 \text{ m}^2 \text{ s}^{-2}$, and the root mean square eddy velocity is $\sim 14 \text{ m s}^{-1}$ (Peixoto and Oort, 1992). The remarkable thing is that Jupiter maintains this dynamical activity with only 5% of the power per unit area (13.5 W m^{-2} emitted longwave radiation vs. 240 W m^{-2} for Earth). Given the large winds on Jupiter, perhaps one should not be surprised

that the conversion from eddy kinetic energy to zonal mean kinetic energy is large.

5. Tests for systematic errors

The correlation between $d\bar{u}/dy$ and $\overline{u'v'}$ could potentially be introduced as a by-product of the analysis. We have considered and investigated several possible non-physical sources for the observed correlation.

5.1. Erroneous matches made by feature tracker

An automatic feature tracker can be fooled in ways that humans are not, resulting in possible spurious matches. In this section, we define false matches as matches easily identified as incorrect by the human eye. These tend to involve the feature tracker jumping between similar-looking features. As these false matches tend to involve large jumps, they could potentially have a significant impact on u' or v' . To investigate whether false matches could be the cause of the correlation between $\overline{u'v'}$ and $d\bar{u}/dy$, we employed several checks. Firstly, as mentioned in Section 3.1, all matches were checked by the feature tracker and later screened by comparison with neighboring matches. A subset of matches (200) was investigated by eye after these two steps and no false matches were detected. Therefore, we expect our false matches to be less than half a percent of the total number of matches in the final analysis.

In addition, once $\overline{u'v'}$ had been determined for each latitude bin, we viewed all matches for which $u'v'$ was greater than 4σ away from the mean. The total number of such matches was about 2264, which is $\sim 1\%$ of all $u'v'$ measurements. We displayed the left and right images, zoomed in on the correlation box, and blinked the two images. Ten false matches, about half a percent of all high $u'v'$ matches, were identified and removed by this procedure. $\overline{u'v'}$ remained unchanged at most latitudes; at a few latitudes it was changed by up to $1.5 \text{ m}^2 \text{ s}^{-2}$. The correlation coefficient between $\overline{u'v'}$ and $d\bar{u}/dy$ before and after removal of these matches was changed by less than half a percent.

5.2. Uneven sampling

Suppose, for a given latitude, that the actual average eddy momentum flux is 0, but that regions with positive EMF are over-sampled with respect to regions with negative EMF. This could result in $\overline{u'v'}$ values that are much higher than the true mean. To investigate the effects of uneven sampling, we took all (x, y) pairs and averaged them in 1° by 1° boxes before averaging over longitude to determine \bar{u} and \bar{v} . We then calculated (u', v') pairs and averaged their product, $u'v'$, into 1° by 1° boxes before averaging over longitude to determine $\overline{u'v'}$. In this way, every square degree of latitude and longitude receives equal weight. (About 3% of the bins had no matches and were, therefore, not given any weight in this analysis.) A comparison between binned and un-binned analyses can be seen in Fig. 7. The two curves are virtually indistinguishable, demonstrating that uneven sampling is not affecting our results.

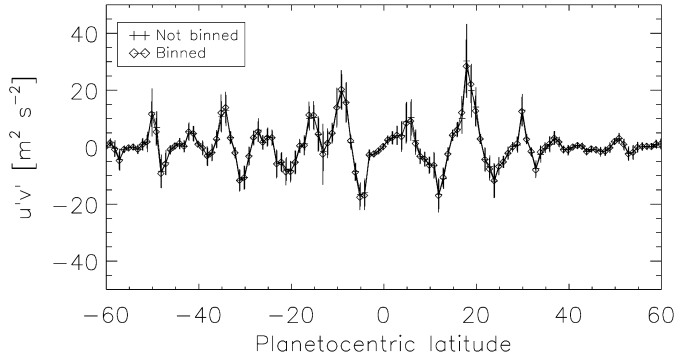


Fig. 7. $\overline{u'v'}$ is plotted as a function of latitude for the initial analysis and for one in which vectors were first binned into 1° by 1° boxes before longitudinal averaging.

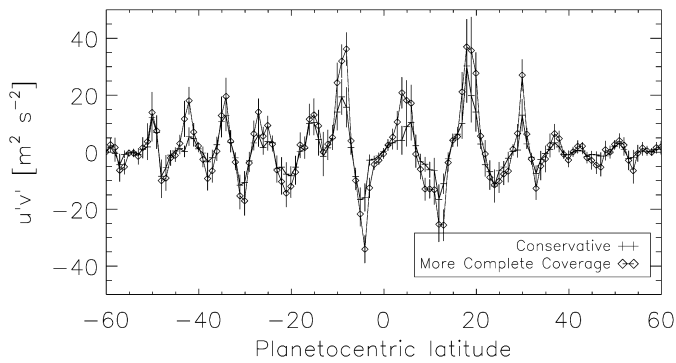


Fig. 8. $\overline{u'v'}$ is plotted as a function of latitude for two different sets of acceptance criteria used in the tracker program. For the initial conservative analysis, the feature tracker only accepted matches in which the correlation coefficient of the match was greater than 0.8, and matches were ‘checked’ (see Section 3.1). For another analysis, which provides more complete coverage of the planet, at the risk of introducing noisier data, the feature tracker accepted matches as low as 0.5 and did not ‘check’ matches. Error bars on $\overline{u'v'}$ represent 2 standard deviations from the mean.

In another test, we attempted to even the sampling coverage by allowing the feature tracker to accept lower correlation coefficients for matches (as low as 0.5) and having it not ‘check’ the matches by working backwards (see Section 3.1). All matches were then screened by comparison with neighbors to remove false matches, as described in Section 3.1. About 8% of matches were eliminated by the screening process. In this analysis, there were very few ‘holes’ in latitude/longitude space. The right-hand side of Fig. 3 shows a sample image with the locations of matches overlaid, demonstrating that the spatial coverage is nearly complete. A comparison of this analysis with more complete coverage and our initial conservative analysis can be seen in Fig. 8. Although the shapes of the two curves are the same, the amplitude of the oscillations in $\overline{u'v'}$ is greater for the more complete coverage. This is probably due to two very different effects. Firstly, the clouds tend to be stretched out and tilted by wind shear (see Fig. 9), so the error for the matches could be greatest in the direction of cloud tilt. These errors may mimic the effect of diagonal motion and should be more apparent in the more complete analysis. This effect is discussed further in Section 5.5. Secondly, if high $\overline{u'v'}$ values are found frequently in visually chaotic areas, some of the matches in these areas

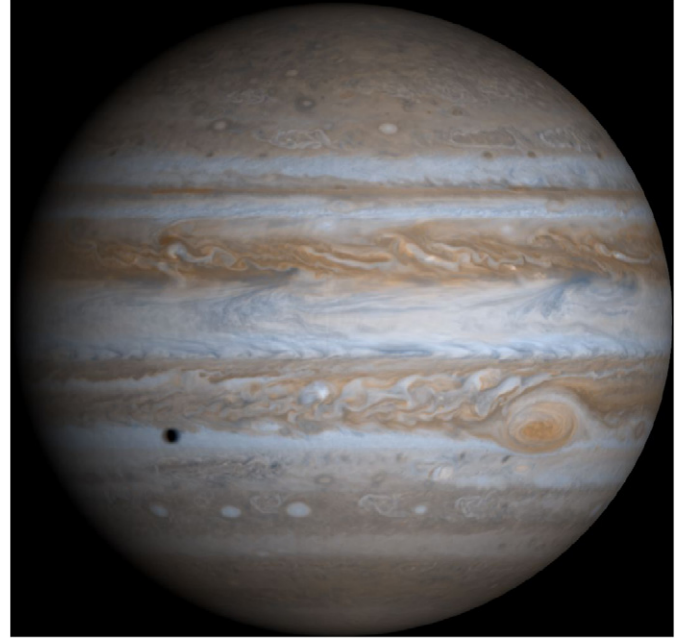


Fig. 9. This whole-disk, true-color simulated image of Jupiter demonstrates how clouds are tilted by the shear in the two prominent dark bands on either side of the equator. In the South Equatorial Belt, the clouds are oriented in the NE/SW direction by a pair of currents, one flowing westward over the northern edge of the Great Red Spot and the other, further north, flowing eastward. In the North Equatorial Belt, the clouds are oriented in the NW/SE direction by a pair of currents with shear in the opposite direction from that in the south. This image is composed of 4 Cassini images taken on December 7, 2000 (NASA photo PIA02873).

may have been eliminated in the more conservative analysis. In other words, some real signal was probably eliminated in the more conservative analysis.

5.3. Biased sampling of large circulating eddies (ovals)

Let us assume that the large oval eddies (such as the Great Red Spot) contribute no net momentum to the zonal flow. If ovals are preferentially sampled, for example, in their northeast and southwest corners, it may appear as if they are transferring horizontal momentum to the jets, though they are not, a point made by Sromovsky et al. (1982). To investigate whether this sampling bias was affecting our results, we repeated the analysis after masking out large visual ovals. A total of more than 1100 regions were masked out (representing about 275 individual ovals, since the planet underwent 4 rotations). The masked-out area represented about 10% of the image area used in the full analysis. A comparison of the two results can be seen in Fig. 10. There is a slight change in the value of $\overline{u'v'}$ at its peaks, demonstrating that some ovals may have been unevenly sampled. However, the overall magnitude and character of the curves is unchanged by the removal of ovals.

5.4. Regional and temporal variability

To test the robustness of our results, we split our dataset, performed our analysis on each half and compared. We chose

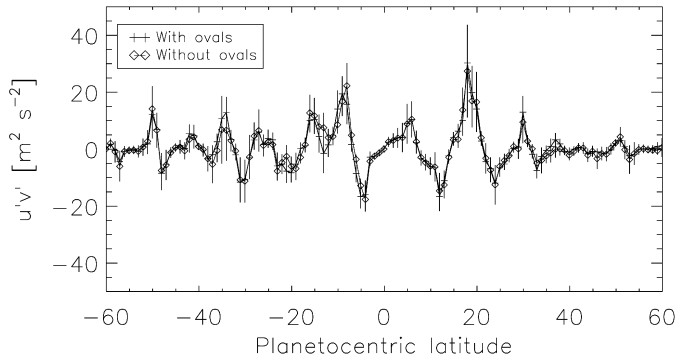


Fig. 10. $\overline{u'v'}$ is plotted as a function of latitude for two analyses—one which included large ovals and one which excluded these regions. Note that the two analyses have slightly different values at the peaks of the curve, but that the magnitude and character of the two curves is similar. Error bars on $\overline{u'v'}$ represent 2 standard deviations from the mean.

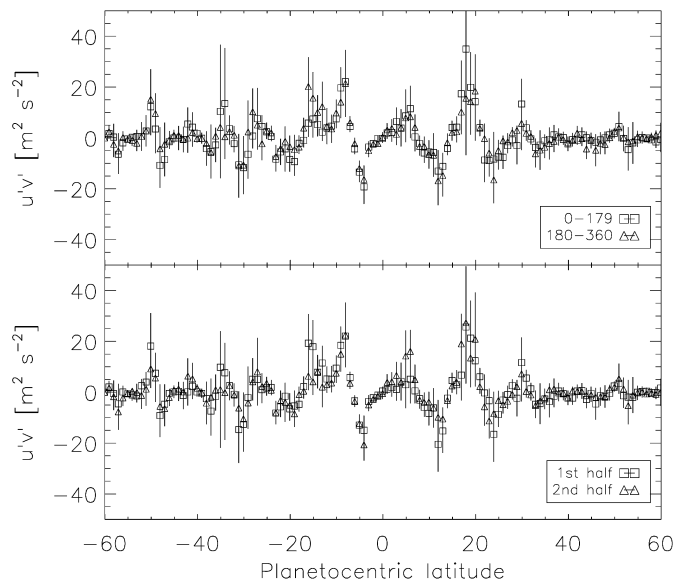


Fig. 11. $\overline{u'v'}$ is plotted as a function of latitude for analyses performed on our dataset split by longitude (above) and time (below). Error bars represent 2 standard deviations from the mean. The analyses agree well, except for some differences at a level consistent with the error bars.

to exclude regions with large ovals, such that the remaining portions of our images should be quite similar, no matter how the data are split. We split our dataset in two ways: by longitude, and by time. A comparison of $\overline{u'v'}$ derived from each of the analyses can be seen in Fig. 11. In general, the datasets appear quite consistent, giving us confidence that our results are robust.

5.5. Anisotropic measurement error

Uncertainties for matches are not the same in all directions. Jupiter's clouds are tilted and stretched by wind shear. When the shear is clockwise, clouds are tilted from NE to SW; when the shear is counterclockwise, the reverse is true (see Fig. 9). The feature tracker therefore encounters greater position uncertainty along the direction in which the clouds are stretched than in the perpendicular direction, because most of the contrast oc-

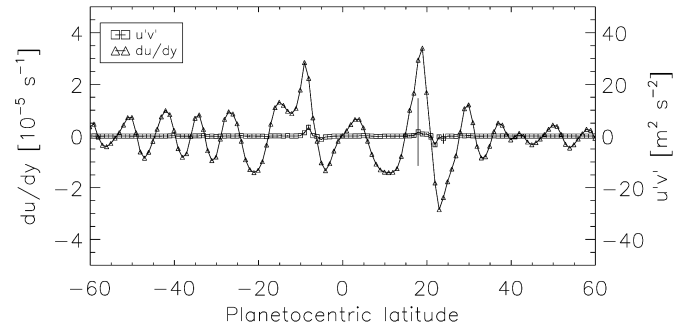


Fig. 12. $\overline{u'v'}$ and $d\bar{u}/dy$ both plotted as a function of latitude for our analysis of artificially sheared images. A significant $\overline{u'v'}$ signal appears because of the errors induced by the shear, although it is isolated to the few areas with the greatest degree of shearing. Error bars on $\overline{u'v'}$ represent 2 standard deviations from the mean.

curs at cloud boundaries. If a feature is mis-identified along the cloud direction it will appear to have a u' and v' tilted in the direction of the cloud, whose orientation is in-turn set by $d\bar{u}/dy$. This should cause a purely measurement-induced correlation between $\overline{u'v'}$ and $d\bar{u}/dy$. To determine the magnitude of such an effect, we created artificial image pairs for which $\overline{u'v'}$ should be zero and repeated our analysis with these pairs. The artificial pairs were created by using 58 images and artificially shearing them both backwards and forwards according to the zonal wind pattern of Fig. 4 and assuming that they were separated by the same period of time (just over 9 h) as the real image pairs. Flux errors in our actual images were small, but natural feature variation in Jupiter's atmosphere can significantly affect the ability of the tracker to follow features. Therefore, to mimic uncertainties introduced by changes in feature shapes and brightnesses that would occur in real image pairs, but are not present in our artificially created pair, we added different, unrelated images from our set at the 10% brightness level to each of our images. The images were analyzed with the feature tracker, using the same parameters as for the analysis with more complete coverage, and subjected to all of the same analyses as the real images. Since the process of making these artificial pairs did not introduce any North–South displacement, if there were no directionality to the feature-matching process, the measured $\overline{u'v'}$ would be zero.

The results of this analysis can be seen in Fig. 12, where we have plotted $\overline{u'v'}$ and $d\bar{u}/dy$ as a function of latitude. Although there is no intrinsic motion in the y direction, there is a distinct $\overline{u'v'}$ at a few locations of highest shear caused purely by the anisotropic measurement error. This result calls into question the significance of some of the largest peaks in Fig. 5. However, it is interesting to note that the measurement bias only affects the analysis in the locations of highest shear; elsewhere, $\overline{u'v'}$ is basically zero. In addition, the correlation coefficient between $\overline{u'v'}$ and $d\bar{u}/dy$ is only 0.56. Most importantly, however, although a correlation between $\overline{u'v'}$ and $d\bar{u}/dy$ exists, the power transfer that would be inferred from this correlation is at least an order of magnitude less than that in the real analysis (see Table 1).

We also tested the importance of the time difference between the synthetic pairs and the degree of added noise. The time dif-

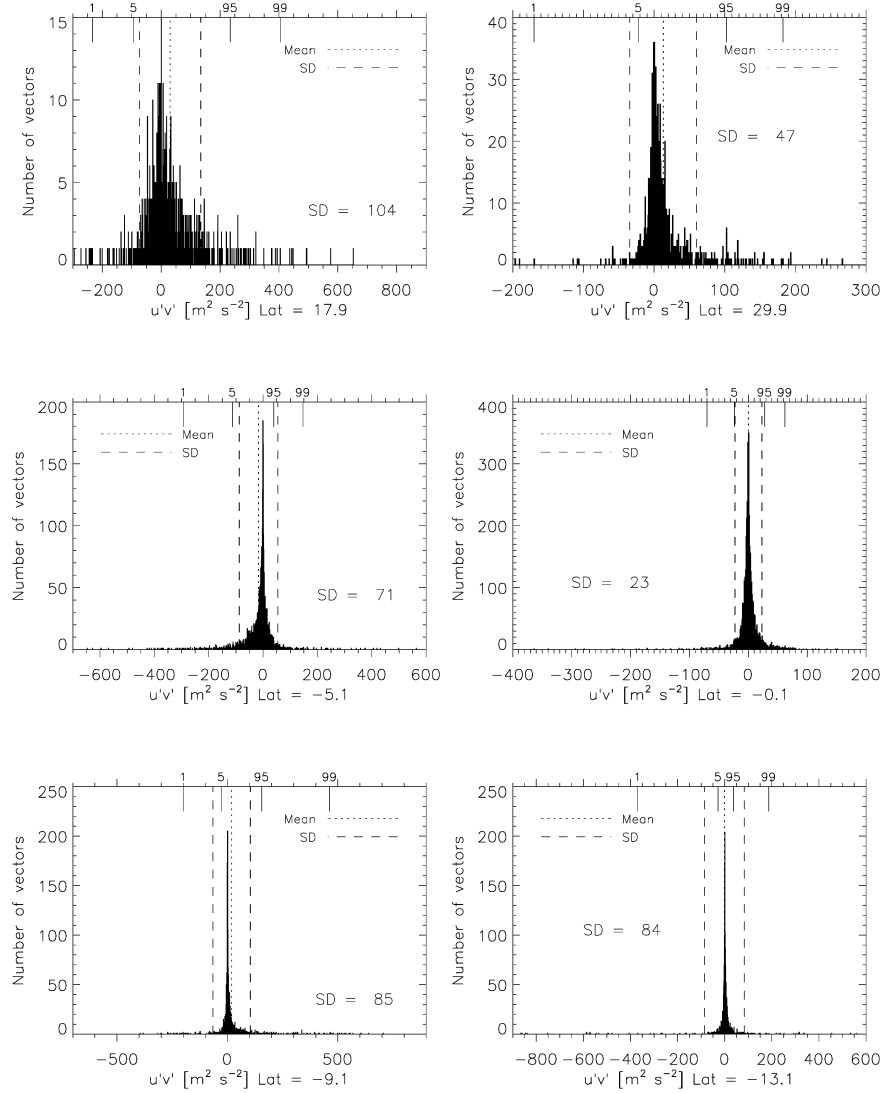


Fig. 13. Histograms of $u'v'$ values from the nominal analysis are shown for 6 latitude regions. Four histograms come from latitudes that correspond to peaks in Fig. 5; the other two (lat = -0.1 and lat = -13.1) correspond to $u'v'$ near zero. Tick marks above the plot mark the points at which 1, 5, 95 and 99 percent of the data lie to the left. These histograms demonstrate the non-normality of the $u'v'$ values. Note particularly that for the latitudes that correspond to the peaks in Fig. 5, the mean (shown by a dotted line) does not correspond to the peak of the histogram but is shifted in the direction of the longest tail of the distribution. The standard deviation of the dataset at each latitude is shown both graphically and numerically.

ference was varied from between 0.25 and 1.5 times the time difference between the real image pairs (i.e. between 2 and 14 h). In all additional tests, the magnitude of the $\overline{u'v'}$ signal was lower at the location of the peaks seen in Fig. 12. For the case with the greatest time separation, small peaks appeared at a total of about 5 locations of high $|d\bar{u}/dy|$; however, the magnitude of the peaks was generally significantly smaller than in the real analysis. The noise was also varied from 0 to 20%. In all cases, the $\overline{u'v'}$ signal was similar to that seen in Fig. 12. In all of our synthetic tests, a false $\overline{u'v'}$ was induced, but in no case did it have the magnitude and shape of that seen in the real images, nor did it ever appear at all of the latitudes at which it was seen in the real analysis. Therefore, while measurement uncertainty alone may account for some of the observed correlation between $d\bar{u}/dy$ and $\overline{u'v'}$, it does not account for all of the correlation.

5.6. Non-normal distributions

In a given latitude bin, the individual $u'v'$ values do not cluster symmetrically and normally about the mean, $\overline{u'v'}$. The $u'v'$ distributions have large, asymmetric tails that have a strong influence on $\overline{u'v'}$. In Fig. 13, we show histograms of $u'v'$ values at several latitudes. In Fig. 14, we show analyses in which we eliminated the tails of the distributions and recalculated $\overline{u'v'}$. It is possible that the non-normal behavior is an artifact of the analysis. We know they are not obviously erroneous matches because, as discussed in Section 5.1, outliers in the $u'v'$ distribution were visually inspected to confirm that the feature-tracker was doing its job correctly. However, non-normal distributions are also seen at the high-peak latitudes in the analysis of artificially sheared images. Therefore, there is some possibility that the tails may somehow be related to the anisotropic measure-

ment uncertainties. Another possibility is that the tails represent the uneven sampling of large ovals. However, we believe this is unlikely, given that the removal of all large visual ovals did not greatly affect the analysis (see Section 5.3).

It is also possible that the non-normal behavior is real, and not introduced by the analysis. $u'v'$ values need not be normally distributed. In fact, the tails may demonstrate that momentum

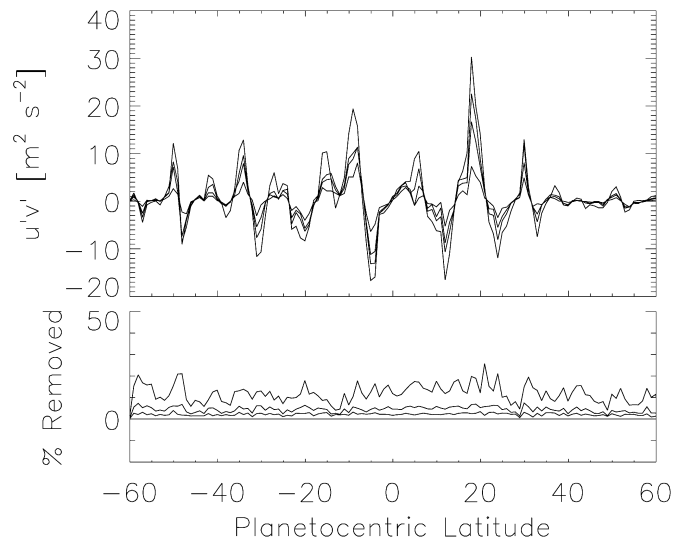


Fig. 14. To test the importance of outliers in the distributions seen in Fig. 13, we eliminated the tails of the distributions and recalculated $\overline{u'v'}$. In three separate analyses, $u'v'$ values beyond 1, 2 or 3 standard deviations from zero were eliminated from each latitude bin, and $\overline{u'v'}$ was recalculated. (The zero point corresponds closely to the peak of the histogram at all latitudes.) The upper plot shows $\overline{u'v'}$ vs. latitude for these three analyses as well as for the nominal analysis in which all points were included. The absolute magnitude of $\overline{u'v'}$ decreases with increasing amounts of excluded data, demonstrating that the datasets are highly asymmetric about zero and outliers have a significant impact on $\overline{u'v'}$. The lower plot shows the percentage of data removed at each latitude for these same four analyses, with the nominal case at the bottom and the 1 standard deviation case at the top.

is preferentially transferred by eddies in a few localized regions, rather than evenly throughout the planet's surface. This would not be surprising, as momentum transfer by eddies may be linked to convective activity, and convective activity is observed to occur in localized regions. Little et al. (1999) surveyed an area of $39.5 \times 10^9 \text{ km}^2$ and observed 26 lightning storms ranging in size from 99 to 1695 km. Thus the fractional area occupied by lightning storms is in the range 10^{-5} – 10^{-3} . Porco et al. (2003) identified distinct bright regions, which they called “convective regions,” found exclusively in Jupiter’s dark belts. In addition, Li et al. (2004) identified a population of spots characterized by “sudden appearance of a bright point followed by rapid expansion in size,” which they termed “probable convective regions.” Our preliminary analyses show no obvious link between high $u'v'$ values and convective features; however, we believe the locations of high $u'v'$ deserve a closer look. Fig. 15 demonstrates the influence of points with large values of $u'v'$ and gives a sense of the variety of features they correspond to. These include very tilted clouds, bright, busy regions, circular features and non-distinct regions. A complete characterization of the morphology and location of these features may provide or exclude a link to convective or other features.

In short, it is clear that $u'v'$ outliers are playing an important role in our analysis; unfortunately, it is hard to say with certainty what the cause or implication of these tails may be. We leave more extensive analysis of $u'v'$ values, u' and v' themselves, and the relation to feature morphology and time evolution as future work.

5.7. Navigation and tracking errors

There are a couple of ways in which navigation or tracking errors could induce a correlation between $\overline{u'v'}$ and $d\bar{u}/dy$. Since we have found a non-zero value for \bar{v} (see Fig. 4) that is indicative of navigation problems, we consider this issue in some detail. A navigational error capable of causing the

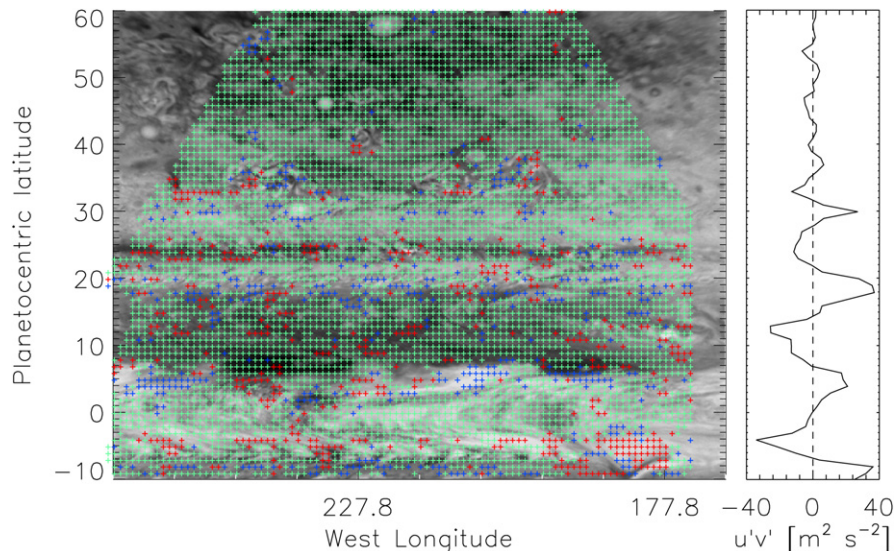


Fig. 15. A portion of a sample map is displayed with match locations overplotted and color-coded according to the value of $u'v'$ at that point. Matches come from the ‘more complete coverage’ analysis. Red points have $u'v'$ less than $-40 \text{ m}^2 \text{ s}^{-2}$, blue points have $u'v'$ greater than 40 and green points have $u'v'$ between -40 and 40. For reference, we include a plot of $u'v'$ (derived from the complete dataset—not from just this image) for the latitudes between 10° S and 60° N .

observed \bar{v} (0.2 m s^{-1}) would only need to be $0.2 \text{ m s}^{-1} \times 34,074 \text{ s}/(124 \text{ km pix}^{-1}) \approx 0.05 \text{ pix}$ per image pair at the equator. An error of this magnitude could easily go undetected throughout much of the analysis.

Both random navigation errors and random feature identification errors can produce a false correlation between $\overline{u'v'}$ and $d\bar{u}/dy$. The sign and magnitude of the correlation depend on how one defines a feature and how one chooses \bar{u} . We use 1° latitude bins and define a single \bar{u} for each bin. Features are whatever clouds lie within our correlation box as it steps along the middle latitude of the bin in the earlier image. The time interval is short enough that the features stay within the latitude bin in the later image. First consider a pair of images in which the latitudes assigned to features in the earlier image are too low because a navigation error has biased the latitude–longitude grid northward by a distance δy , and δt is the time interval between images. If there is no intrinsic northward velocity, the calculated northward velocity will be $\delta y/\delta t$. The eastward velocities will be too high by an amount $\delta y d\bar{u}/dy$, which is the difference between \bar{u} at the feature's true latitude and that at the assigned latitude. Thus a navigation error in the earlier image has a spurious contribution to $\overline{u'v'}$ given by $(\delta y)^2(d\bar{u}/dy)/\delta t$. The correlation between $\overline{u'v'}$ and $d\bar{u}/dy$ is positive, regardless of the sign of δy . A navigation error in the later image does not produce a spurious \bar{u} , so a bias in y does not produce a spurious u' . Biases in x are uncorrelated with v' and the spurious $\overline{u'v'}$ is zero. The same argument applies to feature identification errors in the later image. There are no feature identification errors in the earlier image because the features are defined by whatever clouds are in the correlation box. Thus feature identification errors do not produce a spurious correlation between $\overline{u'v'}$ and $d\bar{u}/dy$.

With our scheme, therefore, feature identification errors do not produce a spurious $\overline{u'v'}$. Navigation errors, on the other hand, do produce a spurious value of $\overline{u'v'}$, and it is given by $(\delta y)^2(d\bar{u}/dy)/\delta t$. We can determine an upper bound on the mean of $(\delta y)^2$ by evaluating \bar{v}_i , which is the average northward velocity of all features in image pair i , for each of the N image pairs. Since each image pair covers several belts and zones, we can assume that the true northward velocity averaged over the image pair is relatively small, i.e., that the measured \bar{v}_i is mostly due to navigation error. Then

$$\overline{(\delta y)^2} \leq \frac{(\delta t)^2}{N} \sum_{i=1}^N (\bar{v}_i^2) = 239 \text{ km}^2. \quad (7)$$

The inequality allows for the possibility that some of the measured \bar{v} is real rather than due to navigation error. The numerical value on the right is the result of our analysis and corresponds to a δy of about a tenth of a pixel or a root mean square velocity of 0.45 m s^{-1} . Using this value with $d\bar{u}/dy = 10^{-5} \text{ s}^{-1}$ and $\delta t = 9.46 \text{ h}$, we find that the spurious $\overline{u'v'}$ is of order $0.07 \text{ m}^2 \text{ s}^{-2}$. This is two orders of magnitude smaller than the typical values that we measure (Fig. 5), so we conclude that random navigation errors of the magnitude seen in our analysis do not produce a significant correlation between $\overline{u'v'}$ and $d\bar{u}/dy$.

Another way to investigate whether the observed \bar{v}_i produces a spurious $\overline{u'v'}$ is to assume \bar{v}_i is all due to navigation error,

correct for it and recalculate $\overline{u'v'}$. With this correction, $\overline{u'v'}$ was changed by, at most, $2 \text{ m}^2 \text{ s}^{-2}$, with a total change to the power per unit mass of less than 2%.

Another possible navigation error is that of a steady tilting of images with time. In this case, however, one would expect to see a correlation of \bar{v} with \bar{u} . With no obvious visual relationship between the two parameters and a correlation coefficient of only -0.19 , it does not appear that our images have tilted with time.

We conclude that navigation and tracking errors are not producing the $\overline{u'v'}$ seen in our analyses.

6. Discussion and conclusions

Utilizing an automatic feature tracker, we have analyzed image pairs from the recent Cassini flyby of Jupiter and find a positive correlation between $\overline{u'v'}$ and $d\bar{u}/dy$. Such a correlation implies that eddies in the visible atmosphere of Jupiter are supplying energy to support the zonal wind structure. Jupiter's clouds appear tilted and stretched by the wind shear, suggesting that there is motion along the tilted clouds and a corresponding $\overline{u'v'}$ that is positively correlated with $d\bar{u}/dy$. However, if the tilt arose by some other means, without motion in the North–South direction, then it could create a false $\overline{u'v'}$ due to anisotropic measurement error. We have tested for this effect using artificially sheared images, and we find that anisotropic measurement error is contributing a spurious signal in some regions, especially between 5° and 10° S and above and below 20° N, where the tilting is most obvious (Ingersoll et al., 1979). However, the real $\overline{u'v'}$ pattern extends as far as we were able to investigate—between the latitudes of 60° S and 60° N. The energy transfer appears to be a ubiquitous process.

Our analysis also shows evidence that peaks in $\overline{u'v'}$ are strongly influenced by values of $u'v'$ far from $\overline{u'v'}$. This may indicate that momentum is being transferred primarily by a small number of small-scale eddies. However, although we might therefore expect an association between such eddies and convective features, we have yet to find evidence for it. An in-depth investigation of outliers in the $u'v'$ distributions may be able to shed light on this issue.

Many justifiable concerns have been raised about the possibility that the correlation between $\overline{u'v'}$ and $d\bar{u}/dy$ arises in the analysis itself and is not representative of physical processes (Sromovsky et al., 1982). We have investigated many possible routes for the introduction of false correlation. We find that for all of our analyses, the correlation persists, although the magnitude of energy transfer estimated from the correlation is affected by such factors as sampling density, noise levels, inclusion or exclusion of oval features and anisotropic measurement error. However, because the extent and character of $\overline{u'v'}$ persists throughout our analyses, much of the signal must reflect physical processes.

We have estimated the power per unit mass transferred between eddies and zonal winds by calculating the product $\langle \overline{u'v'} d\bar{u}/dy \rangle$. For our nominal analysis, this product is equal to $7.1 \times 10^{-5} \text{ W kg}^{-1}$. For our entire set of analyses, this product ranges by about a factor of two, from 7.1 – $12.4 \times 10^{-5} \text{ W kg}^{-1}$ and if part of the signal were artificially introduced, the actual

energy transfer per unit mass could be even less than our most conservative estimate. Our nominal results predict energy transfers at a rate 2–4 times less than that found by Ingersoll et al. (1981). This may represent differences between how the human eye and feature tracker identify features. For example, if the features that are large contributors to the correlation between $\overline{u'v'}$ and $d\bar{u}/dy$ have significant morphological changes during the period between two images, they may not be picked out by the feature tracker. On the other hand, a human eye would identify the feature more easily because it would examine the larger spatial context.

If we utilize our estimates for the energy transfer per unit mass as well as the mass per unit area suggested by Ingersoll et al. (1981), we find that the power transfer between eddies and zonal winds is in the range 4–8% of the total thermal energy emitted by Jupiter.

Acknowledgments

We thank our reviewer Larry Stromovsky for his exceedingly thorough and constructive comments. This research was supported by NASA's Planetary Atmospheres Program and by the Cassini Project.

References

- Atreya, S.K., Donahue, T.M., 1979. Models of the jovian upper atmosphere. *Rev. Geophys. Space Phys.* 17, 388–396.
- Banfield, D., Gierasch, P.J., Bell, M., Ustinov, E., Ingersoll, A.P., Vasavada, A.R., West, R.A., Belton, M.J.S., 1998. Jupiter's cloud structure from Galileo image data. *Icarus* 135, 230–250.
- Beebe, R.F., Ingersoll, A.P., Hunt, G.E., Mitchell, J.L., Muller, J.-P., 1980. Measurements of wind vectors, eddy momentum transports, and energy conversions in Jupiter's atmosphere from Voyager I images. *Geophys. Res. Lett.* 7, 1–4.
- DelSole, T., 2001. A simple model for transient eddy momentum fluxes in the upper troposphere. *J. Atmos. Sci.* 58 (2), 3019–3035.
- Holton, J.R., 2004. *An Introduction to Dynamic Meteorology*, fourth ed. Elsevier, San Diego.
- Ingersoll, A.P., Beebe, R.F., Collins, S.A., Hunt, G.E., Mitchell, J.L., Muller, P., Smith, B.A., Terrile, R.J., 1979. Zonal velocity and texture in the jovian atmosphere inferred from Voyager images. *Nature* 280, 773–775.
- Ingersoll, A.P., Beebe, R.F., Mitchell, J.L., Garneau, G.W., Yagi, G.M., Shu, F.H., 1981. Interaction of eddies and zonal flow on Jupiter as inferred from Voyager 1 and 2 images. *J. Geophys. Res.* 86 (A10), 8733–8743.
- Irwin, P.G.J., Weir, A.L., Taylor, F.W., Calcutt, S.B., Carlson, R.W., 2001. The origin of belt/zone contrasts in the atmosphere of Jupiter and their correlation with 5- μ m capacity. *Icarus* 149, 397–415.
- Kunde, V., Hanel, R., Maguire, W., Gautier, D., Baluteau, J.P., Marten, A., Chedin, A., Husson, N., Scott, N., 1982. The tropospheric gas composition of Jupiter's north equatorial belt (NH₃, PH₃, CH₃D, GeH₄, H₂O) and the jovian D/H isotopic ratio. *Astrophys. J.* 263, 443–467.
- Li, L., Ingersoll, A.P., Vasavada, A.R., Porco, C.C., DelGenio, A.D., Ewald, S.P., 2004. Life cycles of spots on Jupiter from Cassini images. *Icarus* 172 (1), 9–23.
- Limaye, S.S., Revercomb, H.E., Stromovsky, L.A., Krauss, R.J., Santek, D.A., Suomi, V.E., 1982. Jovian winds from Voyager 2. I. Zonal mean circulation. *J. Atmos. Sci.* 39, 1413–1432.
- Limaye, S.S., 1986. Jupiter: New estimates of the mean zonal flow at the cloud level. *Icarus* 65, 335–352.
- Little, B., Anger, C.D., Ingersoll, A.P., Vasavada, A.R., Senske, D.A., Brennan, H.H., Borucki, W.J., Galileo ISS Team, 1999. The Galileo imaging of lightning on Jupiter. *Icarus* 142, 306–323.
- Minnaert, M., 1941. The reciprocity principle in lunar photometry. *Astrophys. J.* 93, 403–410.
- Peixoto, J.P., Oort, A.H., 1992. *Physics of Climate*. American Institute of Physics, New York.
- Porco, C.C., and 34 colleagues, 2005. Cassini imaging science: Initial results on Saturn's atmosphere. *Science* 307, 1243–1247.
- Porco, C.C., and 23 colleagues, 2003. Cassini imaging of Jupiter's atmosphere, satellites, and rings. *Science* 299 (5612), 1541–1547.
- Stromovsky, L.A., Revercomb, H.E., Suomi, V.E., Limaye, S.S., Krauss, R.J., 1982. Jovian winds from Voyager 2. Part II: Analysis of eddy transports. *J. Atmos. Sci.* 39, 1413–1432.
- Vasavada, A.R., and 12 colleagues, 1998. Galileo imaging of Jupiter's atmosphere: The Great Red Spot, equatorial region, and white ovals. *Icarus* 135, 265–275.